
THREE-DIMENSIONAL SIMULATIONS OF ABLATIVE HYDRODYNAMIC INSTABILITIES IN INDIRECTLY DRIVEN TARGETS

M. M. Marinak

S. W. Haan

R. E. Tipton

S. V. Weber

B. A. Remington

Introduction

To model ignition in a National Ignition Facility (NIF) capsule implosion, we must understand the behavior of instabilities that can cause breakup of the pellet shell. During a capsule implosion, shocks that transit the shell cause growth of perturbations at the surface or at an interface because of a Richtmyer–Meshkov type of instability.¹ Following shock breakout, or earlier for a shaped pulse, the low-density ablated plasma accelerates the pusher, and the ablation front is Rayleigh–Taylor (RT) unstable.² Ablation and finite density gradients have the effect of stabilizing the short wavelength modes. Unstable modes present on the outer surface grow and feed through to the inner surface. Once the shell encounters the rebounding shock from the capsule center, it decelerates and the inner surface becomes RT unstable. If perturbations grow large enough, pusher material mixes into the core, degrading implosion performance.

Capsule designs for the NIF depend on ablative stabilization and saturation to prevent perturbations initially present on the capsule surface from growing large enough to quench ignition. The shape of the perturbation is a key factor in determining the amplitude at which its RT growth saturates. Classical RT experiments of an air–water interface and third-order theory carried out by Jacobs and Catton³ demonstrated that for a particular rectilinear wave number $k = (k_x^2 + k_y^2)^{1/2}$, the symmetric square mode ($k_x = k_y$) will start to saturate at the largest amplitude of any mode. Two- and three-dimensional (2- and 3-D) simulations by Dahlburg et al.⁴ revealed the same dependencies in thin foils. Since the 3-D shape affects the perturbation saturation and ultimately capsule performance, a quantitative understanding of 3-D shape effects on perturbation

growth is of considerable interest to inertial confinement fusion (ICF) research.

In this article, we examine the first simulations and experiments to study the effect of 3-D perturbation shape on instability growth and saturation in indirectly driven targets. The first section discusses HYDRA, the radiation hydrodynamics code we developed for these simulations. The subsequent section examines 3-D shape effects in single-mode perturbations in planar foil simulations and experiments. A discussion of the evolution of multimode perturbations on planar foils is followed by a discussion of 3-D simulations of instability growth in Nova capsule implosions.

HYDRA

We developed a new 3-D radiation hydrodynamics code, called HYDRA, to perform these simulations. HYDRA uses a structured mesh and has arbitrary Lagrange Eulerian (ALE) capability. Several forms of equations of state (EOS) are available, including the EOS4 tabular database and the inline quotidian EOS (QEOS). Multigroup radiation diffusion is implemented using tabular opacities. The thermal conduction routine applies conductivities calculated with the model of Lee and More.⁵ HYDRA has an Eulerian interface tracker that allows users to resolve material interfaces while making full use of its ALE capability. “Mixed” zones, which contain one or more material interfaces, are subdivided into separate components. Radiation transport, thermal conduction, and other physical processes are treated separately for all of the components of the mixed zones. The interface tracker allows one to avoid distorted meshes, and the accuracy problems they can cause, even while resolving shear flows.

The capability of coupling several adjacent zones together has been incorporated in HYDRA. This allows greater freedom in zoning without the full additional computational overhead and increased memory requirements associated with an unstructured mesh. This coupling is essential to avoid the small Courant time step limits that would occur, for example, in narrow zones near the center or near the pole of a 3-D capsule implosion simulation. This capability can also be applied in the presence of mixed zones, allowing one to adjust the local resolution in different directions relative to a material interface.

We developed a technique for treating radiation transport that enables us to run 3-D simulations of a variety of targets with viable computational requirements. The method involves two separate calculations. In the first, we obtain a detailed treatment of the spectrum by using a large number of photon groups while the geometry is approximated. All the detailed spectrum and opacity information is then collapsed into group constants for a small number of photon groups. In the second calculation, these few group opacities are applied in a simulation that treats the detailed spatial variation with use of the diffusion operator. The method yields estimates of the group opacities that are vastly superior to those obtained with the standard Rosseland mean. Compared with the standard method, this new development has enabled us to perform highly accurate numerical solutions at a small fraction of the computational expense. The implementation of this method, combined with the high run speeds and reduced memory requirements attainable with algorithms written on a structured mesh, make HYDRA well suited for a variety of problems that contain some degree of symmetry.

Shape Effects

Single-Mode Perturbations on Planar Foils

We first examine foils having single-mode rectilinear perturbations $\psi = a \cos(k_x x) \cos(k_y y)$, with $k_x = k_y$, $k_x = 3k_y$, and $k_y = 0$ (2-D). Each perturbation has the same wave number $k = (k_x^2 + k_y^2)^{1/2} = 2\pi/80 \mu\text{m}^{-1}$. To study growth extending from the linear regime through the late nonlinear stage, we use a hypothetical drive that gives a long period of acceleration and thus large growth factors. We take the drive spectrum from a LASNEX hohlraum simulation. The drive temperature history imposed starts with a foot at ~ 100 eV, then ramps up to 162 eV over the first 1 ns and is then held constant through 4 ns. This drive is used for all the planar simulations discussed here except for simulations of Nova experiments. Supertransition array (STA) opacities for CH(Br) are used. The foil is initially 50 μm thick. We use an ideal-gas EOS in this simulation for generality.

Figure 1 shows the evolution of the fundamental mode amplitude of areal density for the three perturbation aspect ratios listed above. Since each perturbation has the same wave number and is initialized with the same amplitude, each should grow at the same rate during the shock transit and early acceleration phases when the perturbation is linear; Fig. 1 shows that this is the case. The two shocks generated during the foot and subsequent rise to the peak of the drive coalesce as they break out of the foil at 1 ns. After a period of linear RT growth, the point at which each mode begins to saturate shows a clear progression with the mode shape. As the mode shape is varied from the least symmetric 2-D mode to the most symmetric 3-D square mode, the

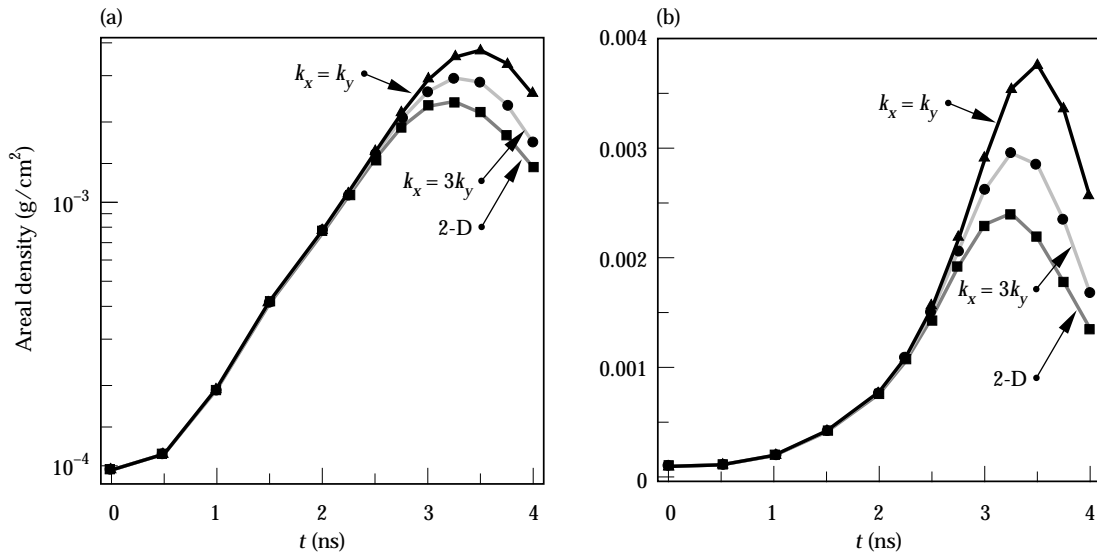


FIGURE 1. Evolution of the fundamental Fourier mode of areal density for three Cartesian mode simulations. Mode amplitudes are plotted (a) on a logarithmic scale and (b) on a linear scale; symbols indicate calculated points. (50-05-0595-1109pb01)

perturbation begins to saturate later and achieves a larger amplitude. The 3-D square mode reaches a peak amplitude 56% larger than the 2-D mode.

Figure 2 shows the $\rho = 0.3 \text{ g/cm}^3$ isodensity surface at 3.25 ns for the 3-D square and 2-D modes. In the nonlinear phase, the 3-D square mode has evolved into a broad bubble surrounded by narrow spikes and adjoining spike sheets. The peak-to-valley (p-V) displacements of the isodensity contours are very similar between the 2- and 3-D modes. The larger amplitude of the square mode is manifest primarily because of its greater density in the spike.

The hexagonal mode perturbation,

$$\psi = a \left[\cos\left(\frac{k_0 x}{2}\right) \cos\left(\frac{\sqrt{3}k_0 y}{2}\right) + \cos(k_0 x) \right], \quad (1)$$

consists of a hexagonally packed array of either bumps or pits, depending on the sign of the perturbation. Reversing the sign of this mode results in a different shape, not just a shift in the phase. Simulations of foils with the two orientations of hexagonal-mode perturbations show rather different evolution in the nonlinear regime. The bubble-centered orientation, consisting of an array of pits, develops into hexagonal bubbles surrounded by spike sheets in the nonlinear stage as shown in Fig. 3(a). The spike-centered orientation, shown in Fig. 3(b), develops isolated individual spikes. The maximum p-V areal density modulations obtained are $45.3 \text{ g } \mu\text{m/cm}^3$ for the bubble-centered perturbation and $83.8 \text{ g } \mu\text{m/cm}^3$ for the spike-centered perturbation. Growth of the spike-centered mode is favored on the ablating foil because it has a smaller surface area subject to ablation and because more material surrounds the base of the axisymmetric spike. The bubble-centered

FIGURE 2. Isodensity plots for $\rho = 0.3 \text{ g/cm}^3$ at 3.25 ns: (a) for the simulations of the $k_x = k_y$ square mode and (b) for the $k_y = 0$ (2-D) mode. One period of the perturbations is shown ($k = 2\pi/80 \text{ } \mu\text{m}^{-1}$). For each plot, the perspective is from the side of the target ablated by x rays. (50-05-0595-1110pb01)

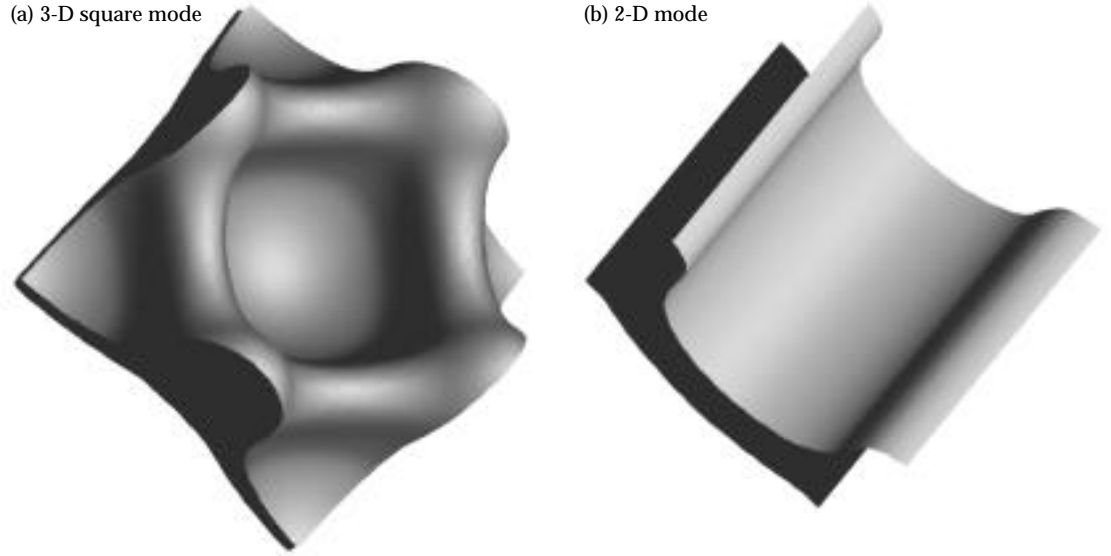
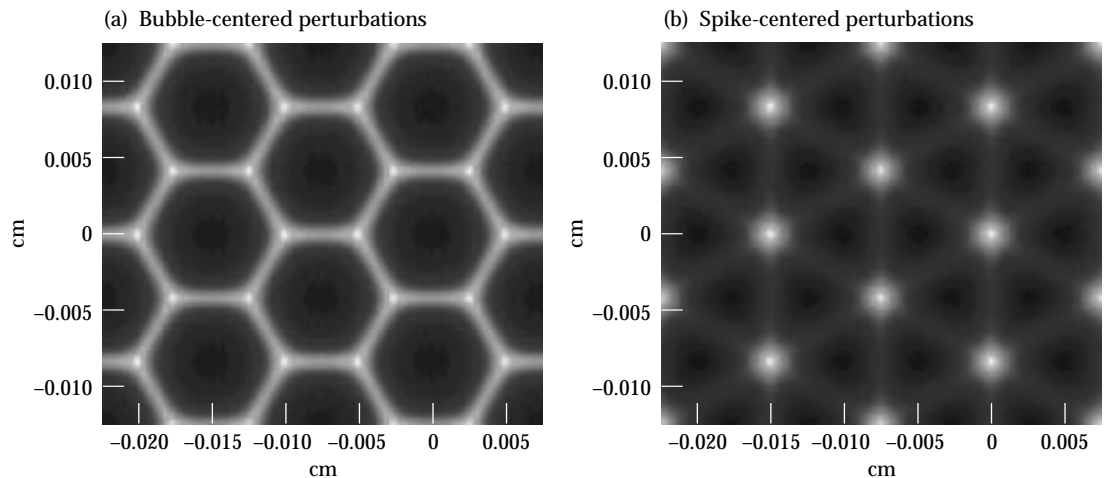


FIGURE 3. Plots of areal density for the two hexagonal-mode orientations in the saturated regime. (a) Bubble-centered perturbations; (b) spike-centered perturbations. Brightest regions correspond to spikes. (50-05-0595-1167pb02)



perturbation attains smaller minimum areal density, and it burns through the foil faster. The axisymmetric bubble is the perturbation shape most dangerous to the survival of thin capsule shells.

3-D Shape Effects in Experiments

We performed an experimental study of single-mode shape effects with planar foils on Nova. In this article, we consider some of these results and compare them with simulations. For these experiments, surface perturbations are molded onto one side of a CH(Br) foil ($C_{50}H_{47}Br_{2.7}$) 750 μm in diameter, 53–57 μm thick, density 1.26 g/cm^3 . The foil is mounted across a hole in the wall of a 3000- μm -long, 1600- μm -diam Au cylindrical hohlraum with the perturbations facing inward. It is illuminated from the back by a 500–700- μm -diam source of “backlighter” x rays created by irradiating a disk of either Rh or Sc with one or two Nova beams. We use measurements of the transmitted intensity of backlighter x rays to determine the growth in the areal density of the perturbations. For targets with 2-D perturbations, a time-resolved image $I(x,t)$ is recorded onto film using a 22 \times magnification streaked Wölter x-ray microscope⁶ with a Rh backlighter. For foils with 3-D perturbations, we collect gated images $I(x,y,t)$ at several times during the shot using the flexible x-ray pinhole imager (FXI)⁷ in conjunction with a Sc backlighter. We characterized the spatial resolution of these instruments and included it wherever simulations are compared with data.

Eight 0.351- μm , 2.2-kJ shaped Nova beams irradiate the hohlraum. The shaped drive, termed laser pulse shape 23, has a low-intensity ~ 1.5 -ns foot, which is followed by a rapid increase to peak power at 2.5–3.0 ns with a peak-to-foot intensity ratio of 10. Our most recent model of this x-ray drive is based on a 2-D LASNEX Au hohlraum simulation. During the foot of the pulse ($t < 2$ ns), we increase the preheat portion of the spectrum ($h\nu > 1.4$ keV) by a factor of 10 over that predicted by LASNEX while maintaining the same total power in the drive. The result is that during the foot an average of 8% of the total energy in the drive spectrum is above 2 keV. This adjustment stems from uncertainty in the total preheat energy deposited in the foil early in time. It has the effect of reducing growth somewhat, systematically improving the fit throughout the database. This drive model reproduces well the foil trajectories and thus the zero-order hydrodynamics.⁸

We examine the effect of perturbation shape on saturation amplitude by comparing a foil having a square-mode perturbation ($k_x = k_y$) with one having a 2-D perturbation ($k_y = 0$), each having the same effective wave number $k = 2\pi/50 \mu\text{m}^{-1}$ and similar amplitudes. We used a laser ablation technique to create the periodic 3-D perturbation on the mold.⁹ With the relatively

short acceleration period of pulse shape 23, large initial amplitudes are required to allow the foils to evolve well into the nonlinear regime. Fourier analysis of an x-ray radiograph of the square-mode foil yields the initial amplitude of the fundamental perturbation as 2.7 μm . Small-amplitude higher harmonics are also present, but their amplitudes are typically less than 10% of the fundamental mode amplitude. The foil with the 2-D perturbation had an amplitude of 2.5 μm . In the HYDRA simulation of the square-mode foil, the surface perturbation initialized includes the predominant $\cos(k_x x) \cos(k_y y)$ modes as well as $\cos(mk_x x) \cos(nk_y y)$ modes having $(m,n) = (0-3,0-3)$ taken from the radiograph.

Figure 4(a,b) compares images of $\ln(\text{exposure})$ calculated from the simulation and measured with the FXI at 4.3 ns, including the effect of instrumental resolution. At this time, the mode has progressed well into the nonlinear phase. The HYDRA simulation reproduces well the structure of the dark narrow spikes, adjoining spike sheets, and wide bubbles. A slight elongation of the central spike is due to the small asymmetry present in the initial perturbation, contained in higher harmonic modes. Figure 4(c,d) makes the same comparison as surface plots of $\ln(\text{exposure})$ vs (x,y) , where the bubble is centered instead of the spike.

Figure 5(a) compares the measured time evolution of the fundamental modes for the 2- and 3-D foils with results from simulations. The data represented by the solid squares and open circles correspond to the $\cos(k_x x) \cos(k_y y)$ components of the Fourier transform of $\ln(\text{exposure})$ for the $k_x = k_y$ perturbation. The open diamond symbols represent the amplitude of the $\cos(k_x x)$ 2-D perturbation. Curves from the HYDRA simulations match well the time evolution of the data. The 3-D mode saturates later at a larger amplitude, consistent with our expectations. Figure 5(b) compares higher harmonics of measured growth factors in Fourier amplitude of $\ln(\text{exposure})$ with values from the simulation of the square mode. Observe that mode (0,2) reverses sign at 3.8 ns as a consequence of mode coupling. Despite initially having different signs, the amplitudes of modes (0,2) and (2,0) tend to converge later in the nonlinear regime as the perturbation evolves toward a more symmetric shape. This dynamic evolution shows that the growth of the most symmetric 3-D shape is favored in the saturated regime.

Our results are consistent with the notion that the saturation amplitudes are a consequence of the mode shape. The calculated flow carries material away from the more spherical 3-D bubble on all sides, allowing it to transit more easily into the spike regions. The resulting faster growth for the 3-D bubble-spike pattern increases the rate of mass flow into the spikes relative to the rate at which it is consumed by ablation, allowing the 3-D square mode to achieve a larger peak amplitude.

FIGURE 4. (a) Contour plot of $\ln(\text{exposure})$ from the simulation at 4.3 ns for one period on the $k_x = k_y$ foil. Dark regions have low exposures, corresponding to high areal density. The effect of the instrument resolution function has been included. The FXI image (b) has been averaged over an area encompassing 4×4 periods on the foil. (c), (d) The same numerical and experimental results are displayed in the form of 3-D surface plots in which the height is proportional to intensity. (50-05-0595-1116pb01)

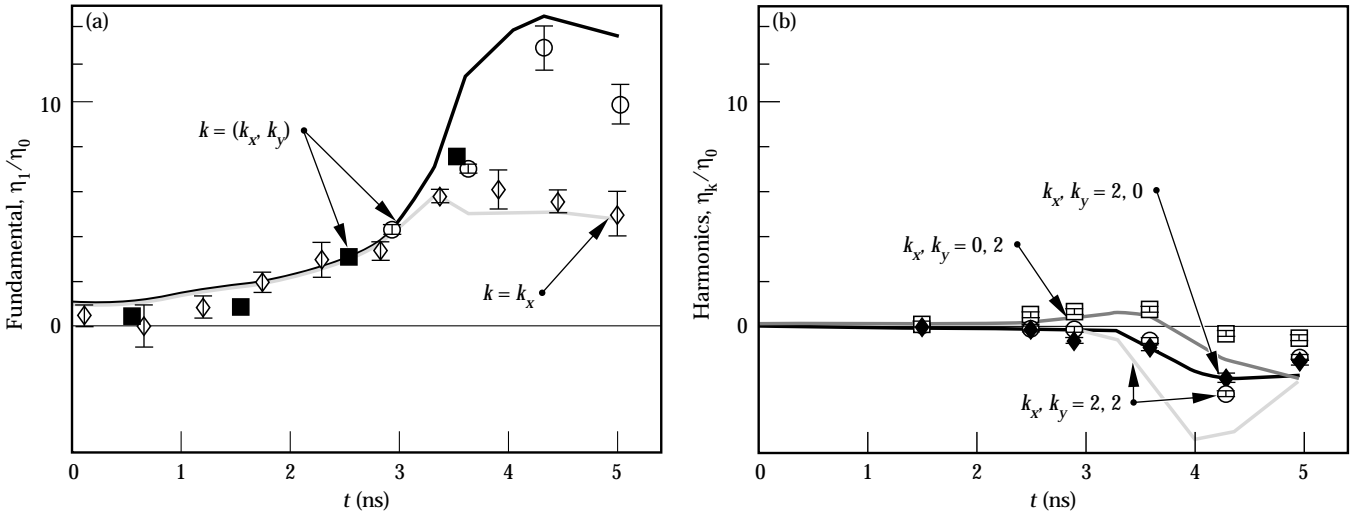
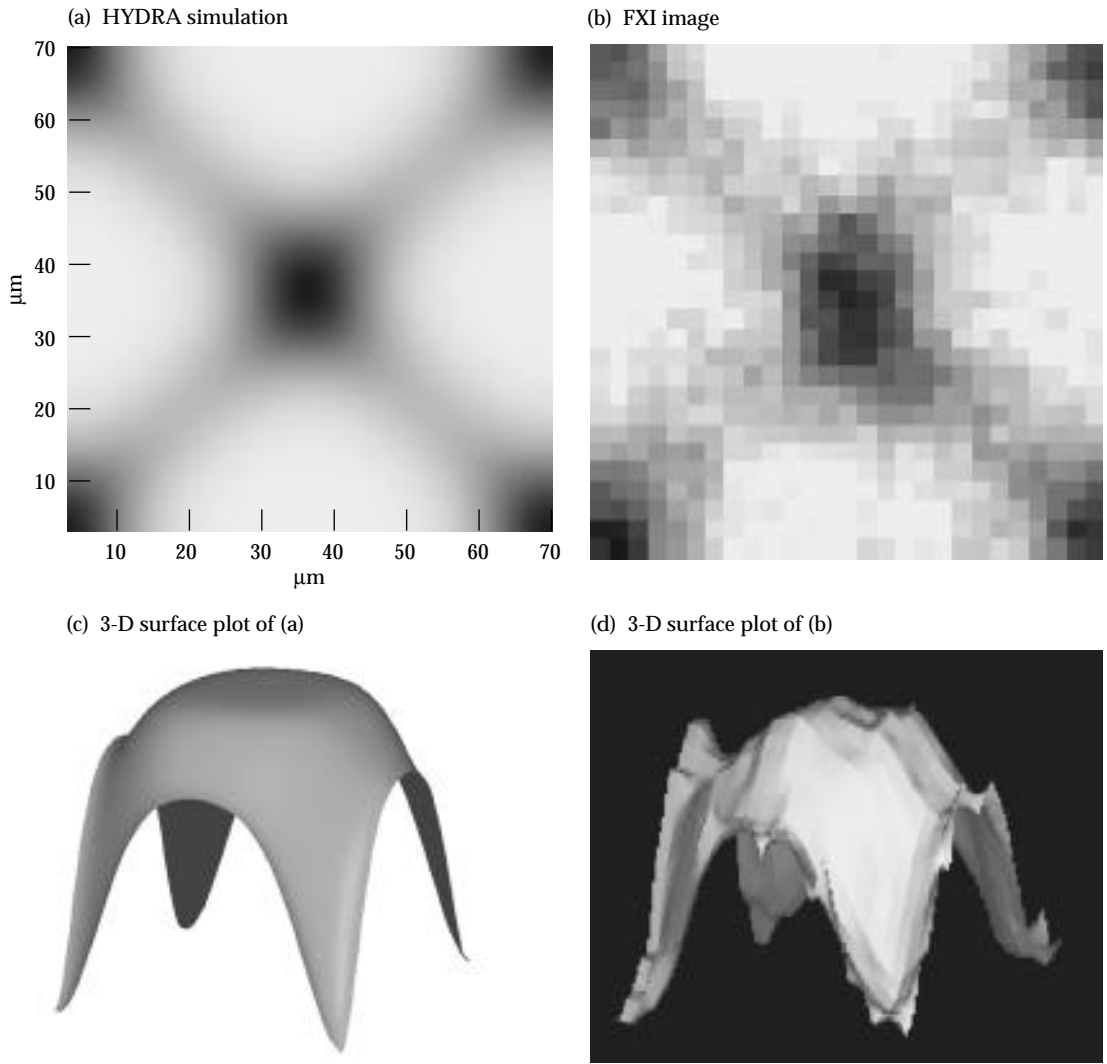


FIGURE 5. Measured and simulated perturbation Fourier amplitudes vs time, normalized to the fundamental mode amplitude at $t = 0$. (a) The solid squares and open circles represent the measured growth factor of $\ln(\text{exposure})$ of the fundamental $k_x = k_y$ mode. The open diamonds are the same quantity for the 2-D mode. The curved lines are the corresponding results from HYDRA simulations. (b) The open circles, solid diamonds, and open squares correspond to the square-mode higher harmonics (2,2), (2,0), and (0,2), respectively. The curved lines give the corresponding simulation results. Experimental error bars represent the corresponding magnitude of the background level in Fourier space. (20-03-0395-0791pb02)

Multimode Perturbations on Planar Foils

Capsule implosion experiments currently being performed on Nova examine the growth of surface perturbations created by ablation with an excimer laser.⁹ Each individual perturbation formed by the laser is in the shape of a pit. Many of these pits may be placed randomly on the capsule to create a spectrum that is random for the low- l mode numbers, but the higher modes that form the shapes of the individual pits are not randomly phased. There is some difference between the nonlinear evolution of this perturbation and that for a truly random spectrum of modes.

A planar surface that contains a number of Gaussian perturbations centered at (x_i, y_i) with amplitudes a_i each having identical widths σ is represented as

$$Z(x, y) = \sum_i a_i \exp \left\{ \frac{-[(x - x_i)^2 + (y - y_i)^2]}{\sigma^2} \right\}. \quad (2)$$

We consider a system with reflection symmetry across each boundary. By using the convolution theorem, we obtain the Fourier spectrum:

$$Z(k_x, k_y) = 16\pi \frac{\sigma^2}{L^2} \sum_i a_i \exp \left[\frac{-(k_x^2 + k_y^2)\sigma^2}{4} \right] \times \cos(k_x x_i) \cos(k_y y_i), \quad (3)$$

where L is the foil width. For k_x or $k_y = 0$, the amplitude of the mode coefficient a_i is multiplied by 0.5 when we

express the spectrum in terms of cosine modes instead of complex exponentials.

Consider two similar foils. In the first, the initial perturbation consists of a set of Gaussian bumps (all a_i positive). Figure 6(a) shows a contour plot of the initial areal density. In the second, the signs of all of the a_i are reversed, which is the corresponding pattern formed with Gaussian pits. [A contour plot for this case would be just the reverse of that shown in Fig. 6(a).] Figure 6(b) is a contour plot of the areal density at 5.0 ns, in the saturated regime, for the first case (Gaussian bump perturbations). The individual bumps have evolved into spike sheets surrounding bubbles. Figure 6(c) shows the nonlinear stage for the second case (Gaussian pit perturbations) at 4.5 ns, which also develops broad bubbles surrounded by narrow spike sheets in the nonlinear regime. This bubble-spike structure is characteristic of the nonlinear development of a random multimode foil.¹⁰ In the saturated regime, both foils have very similar values for p-V and rms areal density. The ratio of the spike amplitude to bubble amplitude is usually taken as $1 + A$, where A is the Atwood number, which is ~ 1 here. We define the bubble side areal density as the rms average over all locations at which the areal density is less than the average value. For the foil with the bump perturbations, the ratio of spike side to bubble side areal density is 2 in the saturated regime, a value that is typical for random multimode perturbations as well. But the bubble-centered random Gaussian foil has an rms areal density on the bubble side essentially equal to that on the spike side in the saturated regime. This bubble amplitude is unusually large. Because of its larger bubble growth, the foil with bubble perturbations burns through first, prior to 5.0 ns for this case.

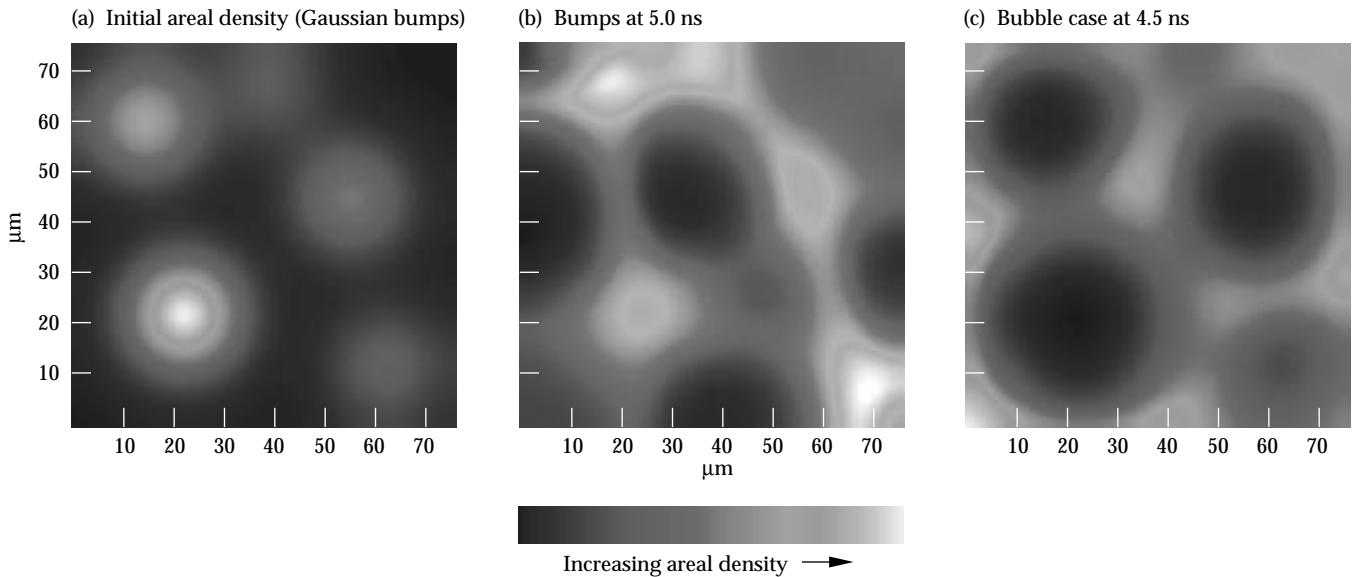


FIGURE 6. Contour plots of areal density for foils with randomly placed Gaussian perturbations. (a) Initial areal density for bumps with various amplitudes. Bumps appear as bright spots. (b) Foil with bump perturbations at 5.0 ns in the saturated regime. (c) Corresponding foil with bubble perturbations at 4.5 ns. (50-05-0595-1111pb01)

The accelerated pace at which the random bubble perturbation burns through the foil is the most significant characteristic distinguishing it from a truly random perturbation.

Next we consider a random multimode foil on which the imposed perturbation

$$\psi = \sum_{m=0}^8 \sum_{n=0}^8 a_{mn} \cos(mk_0 x) \cos(nk_0 y) \quad (4)$$

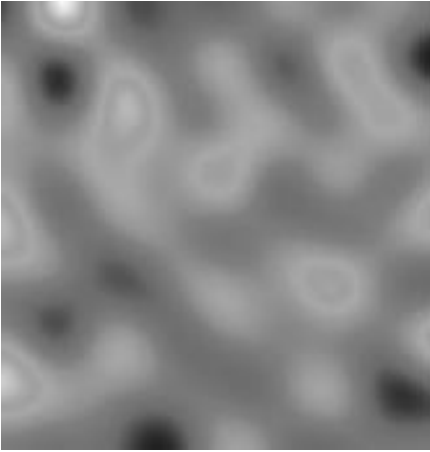
consists of 80 modes with random amplitudes, yielding an initial rms perturbation amplitude of $0.61 \mu\text{m}$ rms. With a fundamental wavelength of $250 \mu\text{m}$, the spectrum of perturbations spans the range of wavelengths most relevant to indirectly driven targets. The foil thickness is initially $50 \mu\text{m}$.

Figure 7(a) shows a contour plot of the initial multimode-foil areal density. The simulation shows that by 2.5 ns [Fig. 7(b)], in the early nonlinear stages of the foil evolution, mode coupling has caused broadening of the

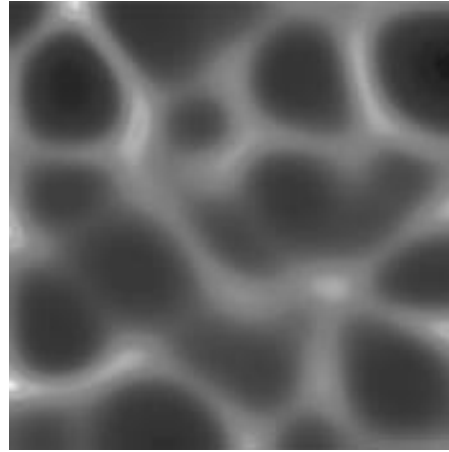
bubbles and the formation of narrow spike sheets. Areal density contours calculated with the Haan second-order mode-coupling theory¹¹ are in good agreement with those from the simulation in the early nonlinear stage. At this time the perturbations still bear some resemblance to those initially on the foil. By 4.0 ns [Fig. 7(c)], strongly nonlinear interactions lead to increased average width of the features. This process is termed *bubble merger* in physical space or *inverse cascade* in Fourier space.

Layzer¹² derived the terminal-rise velocity of a bubble in a semi-infinite incompressible fluid: $u_b = a(g\lambda)^{1/2}$. The Froude number a is 0.23 for a 2-D bubble and 0.36 for a round 3-D bubble. Larger bubbles have less kinematic drag per unit volume, so bubble expansion in the nonlinear regime leads to increasing bubble rise velocities. When driven far enough into the nonlinear regime, substantial displacements develop between bubbles in the longitudinal direction due to the spread in their rise velocities. Some displacement is already apparent in Fig. 8(a), which shows the isodensity

(a) Initial areal density



(b) 2.5 ns areal density



(c) 4.0 ns areal density

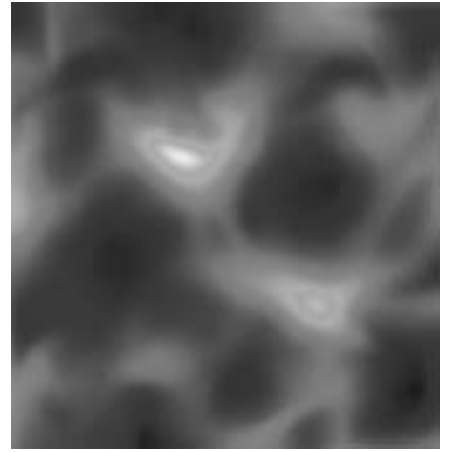
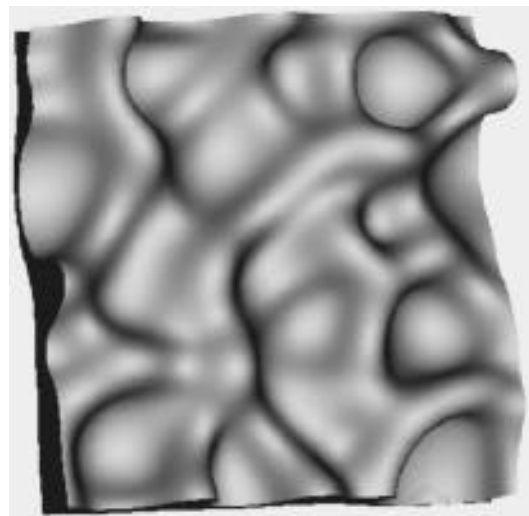


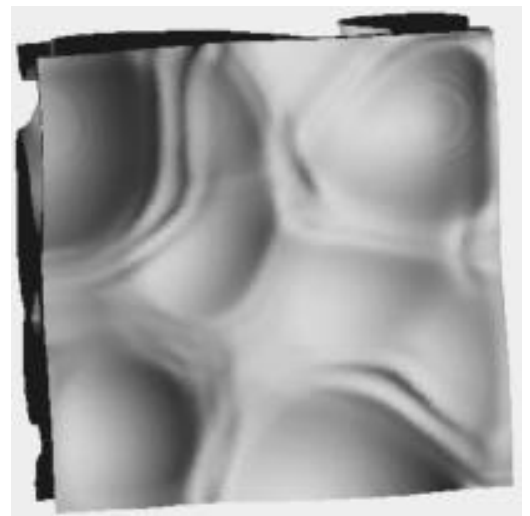
FIGURE 7. Areal density for random multimode foil (a) initially, (b) at 2.5 ns , and (c) at 4.0 ns . Bumps appear as bright spots. (50-05-0595-1112pb01)

FIGURE 8. (a) Three-dimensional plot of 0.75 g/cm^3 density surface at 2.5 ns . View is of the side of the foil ablated by x rays. (b) The 0.3 g/cm^3 density surface at 3.0 ns . View is of bubbles on the side of the foil away from the x-ray source. (50-05-0595-1113pb01)

(a) 2.5 ns isodensity surfaces



(b) 3.0 ns isodensity surfaces



surface $\rho = 0.75 \text{ g/cm}^3$ at 2.5 ns, early in the nonlinear stage. As this longitudinal displacement increases, the bubbles tend to expand laterally to fill the available space. As they move ahead of the others, the tips of the largest bubbles become round, minimizing drag and yielding the highest rise velocity. The isodensity surface shown in Fig. 8(b) shows that the largest bubbles have advanced farthest toward the back side of the foil at 3.0 ns. These bubbles are already much broader than the features of the initial foil perturbation.

Figure 9 plots the Fourier spectrum at 0, 2.5, and 4.0 ns. By 2.5 ns, the spectrum peaks at the wave number having the highest linear growth rate. Mode coupling has driven up higher harmonics. By 4.0 ns, the inverse cascade is apparent as the peak of the spectrum shifts to lower wave numbers. The spectrum has the appearance of a turbulent form, with mode coupling transferring spectral power that originates from the growth of moderate wavelengths to shorter, ablatively stabilized wavelengths and to very long wavelengths. There is little change in the ablatively stabilized portion of the spectrum (above 5000 cm^{-1}) during the saturated phase of evolution, after 3.0 ns.

We used the Haan saturation model to predict rms amplitudes of bubbles and spikes in the weakly nonlinear regime arising from isotropic random multimode perturbations.¹³ In the model, individual modes grow exponentially in the linear regime until the modal

saturation amplitude v/Lk^2 is attained. Then the mode growth changes to secular. Rms bubble and spike amplitudes are obtained by summing modal amplitudes in quadrature. A value of $v = 2$ is generally used for the saturation parameter. As shown in Fig. 10, the departure of the rms bubble growth from linear theory in the simulation initially resembles the model predictions for $v = 1$. The simulated bubble areal density soon rolls over because of burn-through of the foil, which is not accounted for in the saturation model. Since the foil is initially only $50 \text{ }\mu\text{m}$ thick, thin-foil effects appear to have an influence on the saturation amplitude. Perturbation growth continues in low-density regions, and thus contributes little to perturbed areal density. Despite thin-foil effects, the onset of saturation is still roughly consistent with the prediction of the Haan saturation model. This increases our confidence that the model can be used to predict rms perturbation amplitudes in the weakly nonlinear regime.

Capsule Implosion Simulations

The experimental program on Nova is beginning to examine instability growth on capsules that have pits ablated at the 92 positions corresponding to the vertices and face centers of the pattern on a soccer ball.⁹ The shape of an individual pit has been characterized experimentally as a superGaussian function

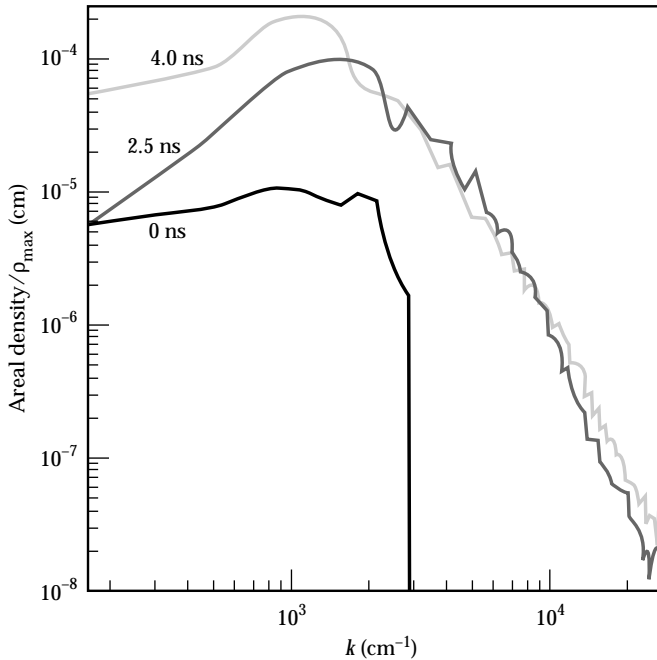


FIGURE 9. Fourier spectra of mode amplitudes vs mode number for multimode foil at 0, 2.5, and 4.0 ns. (50-05-0595-1114pb01)

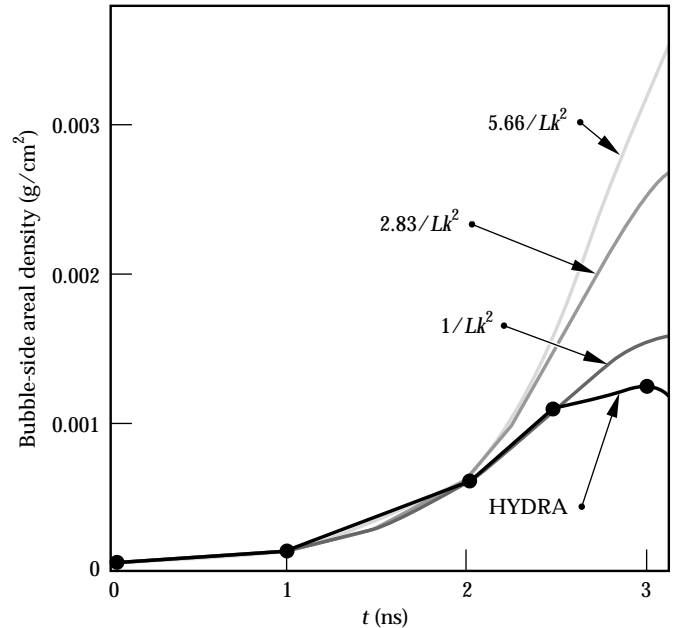


FIGURE 10. The symbols on the solid black line represent the bubble-side rms areal density for the multimode foil calculated with HYDRA. The gray-tone curves represent the bubble-side areal density predicted by the Haan saturation model for three values of the saturation parameter. After 2.5 ns, the values from the simulation begin to roll over because of the effect of finite foil thickness, which is not accounted for in the saturation model. (50-05-0595-1115pb01)

$\psi(r) = -a_0 e^{-(r/\sigma)^3}$ in the radius r , with a_0 the pit depth, and $\sigma = 28 \mu\text{m}$. The overall surface perturbation resulting from these 92 pits can be expressed in terms of the spherical harmonics Y_{lm} :

$$G(\theta, \phi) = \sum_{i=1}^{92} \sum_{l>1}^{\infty} a_l \frac{4\pi}{2l+1} \sum_{m=-l}^l Y_{lm}(\theta'_i, \phi'_i) Y_{lm}(\theta, \phi), \quad (5)$$

where a_l is the coefficient of the Legendre polynomial P_l in an expansion for an individual pit:

$$a_l = \frac{2l+1}{2} \int_0^\pi P_l(\cos \theta) g(\theta) \sin \theta d\theta. \quad (6)$$

Here $g(\theta)$ is the shape function for an individual pit expressed in polar coordinates. For the soccer ball pattern, most of the perturbation is contained in spherical harmonics with $l = 16, 18$. Capsules can also be created with one hemisphere of the pattern rotated by 36° so that the perturbation is reflection-symmetric about the equator. This modification has a minor impact on the mode structure and the spacing between pits. This geometry is treated exactly by simulating $1/20$ of a sphere over a region extending from the pole to the equator and 36° in the azimuthal angle. Symmetry boundary conditions are applied at the transverse boundaries.

The Nova capsules simulated have a fuel region $220 \mu\text{m}$ in radius containing equimolar amounts of H and D. The fuel is bounded by a $3\text{-}\mu\text{m}$ -thick polystyrene mandrel, which is surrounded by a $3\text{-}\mu\text{m}$ layer of polyvinyl alcohol (PVA) and $39 \mu\text{m}$ of Ge-doped polystyrene ablator. We first consider a capsule having pits $0.25 \mu\text{m}$ deep on the outer surface. As the capsule shell accelerates inward, the solid angle occupied by each pit remains essentially constant while it grows into the shell. At the onset of deceleration, isolated bubbles of fuel begin to rise into the shell at the locations of the initial pits, where the fuel column density is lowest, while interconnected sheets of pusher material surrounding these bubbles fall inward. Concurrently, the amplitude of the bubbles on the outer surface begins to decrease. Since the Atwood number at the fuel–pusher interface is ~ 0.4 at this time, shear leads to a Kelvin–Helmholtz instability, causing the material interface to roll up at the tips of the fuel bubbles. The characteristic “hammerhead” shapes are visible in Fig. 11, a plot of the $\rho = 18 \text{ g/cm}^3$ isodensity surface at 2.1 ns . The asymmetric shape of the roll-up, localized near the bubble tip, is due to the bubble-like shape of the initial perturbations. Fuel entrained into the rising bubbles is relatively cool, having temperatures of $\sim 400\text{--}500 \text{ eV}$. Thus significant neutron production arises only from the center of the hot spot in regions

that are many micrometers from spike material. For this $0.25\text{-}\mu\text{m}$ initial perturbation amplitude, the neutron yield is 82% of that obtained with no perturbation. Most of the neutron production has occurred before 2.1 ns .

Simulations have been performed for a range of initial perturbation amplitudes spanning $0.25\text{--}2.5 \mu\text{m}$ p–V. For each of these cases, the perturbation of the fuel–pusher interface becomes nonlinear quite soon after it encounters the first rebounding shock. During the first 100 ps of deceleration, the average bubble rise velocity, defined relative to the interface motion in the unperturbed simulation, exceeds the Layzer asymptotic rise velocity for an axisymmetric bubble in a semi-infinite fluid $0.36(g\lambda)^{1/2}$. The differences between the bubble rise velocities obtained from the simulations and from the Layzer formula increase with the initial perturbation amplitude, becoming substantial for capsules with the larger perturbations. These differences are similar in magnitude to the estimates of linear growth rates for the Richtmyer–Meshkov instability induced by the passage of the first rebounding shock. For example, with an initial $1.25\text{-}\mu\text{m}$ -deep perturbation, the average bubble rise velocity during the first 100 ps of deceleration is $89 \mu\text{m/ns}$. The calculated

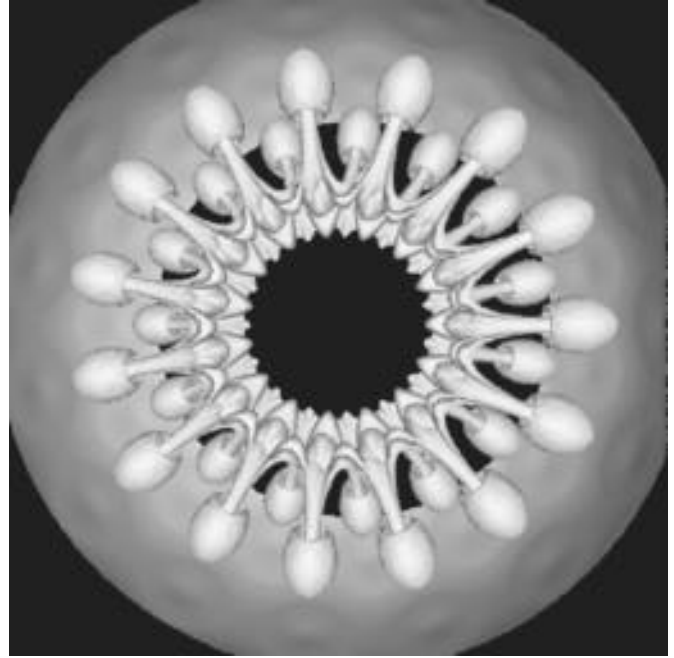


FIGURE 11. Three-dimensional plot of isodensity surface for $\rho = 18 \text{ g/cm}^3$ at 2.1 ns for a Nova capsule with a “soccer ball” perturbation on its exterior. The initial pit depth is $0.25 \mu\text{m}$. Contours are shown over a subset of a hemisphere near the equator. The outer shell is near the ablation region, while the inner surface shown corresponds to the fuel–pusher interface. (50-05-0595-1118pb01)

Layzer rise velocity is $40\text{ }\mu\text{m/ns}$, and the estimated Richtmyer–Meshkov growth rate due to the first rebounding shock is $56\text{ }\mu\text{m/ns}$.

Bubble rise velocities are also affected by spherical convergence, expansion of the rising bubbles, finite shell thickness, and the rise through multiple fluid layers. Further increases are seen later in the bubble rise velocities during a period when they encounter a reflected shock rebounding from the center. The Richtmyer–Meshkov instability clearly has a substantial impact on the perturbation growth during deceleration, particularly on the less massive bubbles. For perturbations in the nonlinear regime, the shocks appear to have a less pronounced effect on growth of the more massive spikes.

As discussed earlier, for a given wavelength a perturbation in the shape of an axisymmetric bubble is able to penetrate the capsule shell fastest. For an initial bubble depth of $2.5\text{ }\mu\text{m}$, the bubble growth in the ablation layer is sufficient to burn through the capsule by the onset of deceleration. As the capsule material ahead of the bubble thins, the bubble tip accelerates inward, forming a highly elongated shape. Doped polystyrene ablator penetrates the PVA and mandrel layers, which are more dense at that time. The resulting spikes of pusher material encounter the rebounding shock $\sim 50\text{ ps}$ sooner than does the fuel–pusher interface in the corresponding unperturbed simulation. The trajectory that the unperturbed interface would follow in the absence of deceleration is termed the fall line. For this large perturbation amplitude, the spike penetrates farther inward, approaching the center of the capsule sooner than the fall line. The neutron production rate is greatly reduced once the spike approaches within several micrometers of the center of the hot spot. Overall neutron yield is only 7.8% of the value obtained for the unperturbed capsule. Nova capsule simulations show perturbation growth causing a large yield degradation only when a spike of pusher material crashes into the center of the hot spot during the period of peak neutron production.

Summary

We examined 3-D growth of ablative hydrodynamic instabilities for a variety of indirectly driven targets. All cases simulated show linear growth rates that are independent of mode shape. For a single-mode rectangular perturbation of a given wave number, the 3-D square mode, which is most symmetric, saturates at the largest amplitude. We verified this for indirectly driven foils through simulation and experiment. Differences in the nonlinear evolution of foils due to perturbation shape are in good quantitative agreement with predictions of the simulations. Of all perturbation shapes, an axisymmetric bubble will burn through a foil the fastest. An isolated axisymmetric spike will attain the largest areal density amplitude.

We simulated a random multimode foil containing perturbations spanning the range of wavelengths of interest for indirect drive. Early in the nonlinear regime, the multimode foil forms broad bubbles and narrow spikes consistent with second-order mode-coupling theory. The onset of multimode saturation is found to be roughly consistent with the prediction of the Haan saturation model. Later, strongly nonlinear interactions lead to an increase in the average width of features. The largest bubbles rise the fastest and continue to grow broader than the initial perturbations.

Simulations of the “soccer ball” capsule show that the positions initially occupied by pits are where fuel bubbles rise during the deceleration phase. A secondary instability at the fuel–pusher interface leads to roll-up at the tips of these bubbles. Most of the neutron production originates in regions that are several micrometers away from any spikes of pusher material. In Nova capsules, mix causes a large reduction in yield only when a spike of pusher material crashes into the capsule center during the time of peak neutron production.

Notes and References

1. R. D. Richtmeyer, *Commun. Pure Appl. Math.* 13, 297 (1960); E. E. Meshkov, *Izv. Akad. Nauk SSSR, Mekh. Ahidk. Gaza* 5, 151 (1969); and G. Dimonte and B. Remington, *Phys. Rev. Lett.* 70, 1806 (1993).
2. J. D. Lindl and W. C. Mead, *Phys. Rev. Lett.* 34, 1273 (1975).
3. J. W. Jacobs and I. Catton, *J. Fluid Mech.* 187, 353 (1988), and J. W. Jacobs and I. Catton, *J. Fluid Mech.* 187, 329 (1988).
4. J. P. Dahlburg and J. H. Gardner, *Phys. Rev. A* 41, 5695 (1990).
5. Y. T. Lee and R. M. More, *Phys. Fluids* 27, 1273 (1984).
6. R. J. Ellis, J. E. Trebes, D. W. Phillion, J. D. Kilkenny, et al., *Rev. Sci. Instrum.* 61, 2759 (1990); B. A. Remington, S. G. Glendinning, R. J. Wallace, S. Rothman, and R. Morales, *Rev. Sci. Instrum.* 63, 5080 (1992); B. A. Remington and R. I. Morales, *Rev. Sci. Instrum.* 66, 703 (1995).
7. K. S. Budil, T. S. Perry, P. M. Bell, P. L. Miller, et al., "The Flexible X-Ray Imager," Lawrence Livermore National Laboratory, Livermore, CA, UCRL-JC-120837 (1995).
8. B. A. Remington, S. V. Weber, M. M. Marinak, S. W. Haan, et al., *Phys. Plasmas* 2, 241 (1995).
9. R. J. Wallace, R. L. McEachern, and W. W. Wilcox, *ICF Quarterly Report* 4(3), 79, Lawrence Livermore National Laboratory, Livermore, CA, UCRL-LR-105821-94-3 (1994).
10. M. J. Dunning and S. W. Haan, *ICF Quarterly Report* 3(4), 179, Lawrence Livermore National Laboratory, Livermore, CA, UCRL-LR-105821-93-4 (1993).
11. S. W. Haan, *Phys. Fluids B* 3, 2349 (1991).
12. D. Layzer, *Astrophys. J.* 122, 1 (1955).
13. S. W. Haan, *Phys. Rev. A* 39, 5812 (1989).